Sheffield Hallam University

# Ultrahigh energy density in short-range tilted NBT-based lead-free multilayer ceramic capacitors by nanodomain percolation

JI, Hongfen, WANG, Dawei, BAO, Weichao, LU, Zhilun, WANG, Ge, YANG, Huijing, MOSTAED, Ali, LI, Linhao, FETEIRA, Antonio <http://orcid.org/0000-0001-8151-7009>, SUN, Shikuan, XU, Fangfang, LI, Dejun, MA, Chao-Jie, LIU, Shu-Yu and REANEY, Ian

Available from Sheffield Hallam University Research Archive (SHURA) at:

https://shura.shu.ac.uk/28030/

This document is the Accepted Version [AM]

**Citation:**

JI, Hongfen, WANG, Dawei, BAO, Weichao, LU, Zhilun, WANG, Ge, YANG, Huijing, MOSTAED, Ali, LI, Linhao, FETEIRA, Antonio, SUN, Shikuan, XU, Fangfang, LI, Dejun, MA, Chao-Jie, LIU, Shu-Yu and REANEY, Ian (2021). Ultrahigh energy density in short-range tilted NBT-based lead-free multilayer ceramic capacitors by nanodomain percolation. Energy Storage Materials. [Article]

**Copyright and re-use policy**

See http://shura.shu.ac.uk/information.html

**Sheffield Hallam University Research Archive**
http://shura.shu.ac.uk

# Ultrahigh energy density in short-range tilted NBT-based lead-free multilayer ceramic capacitors by nanodomain percolation

Hongfen Ji[a,b#], Dawei Wang[a*#], Weichao Bao[c#], Zhilun Lu[a,d#], Ge Wang[a#], Huijing Yang[a,e], Ali Mostaed[a,f], Linhao Li[a], Antonio Feteira[g], Shikuan Sun[a], Fangfang Xu[c], Dejun Li[h], Chao-Jie Ma[i], Shi-Yu Liu[h*], Ian M. Reaney[a*]

[a]Department of Materials Science and Engineering, University of Sheffield, Sheffield, S1 3JD, UK

[b]Laboratory of Thin Film Techniques and Optical Test, Xi'an Technological University, Xi'an 710032, China

[c]State Key Laboratory of High Performance Ceramics and Superfine Microstructure, Shanghai Institute of Ceramics, Shanghai, 200050, China

[d]The Henry Royce Institute, Sir Robert Hadfield Building, Sheffield, S1 3JD, UK

[e]Department of Physics, Tangshan Normal University, Tangshan 063000, China

[f]Department of Materials, University of Oxford, Oxford OX1 3PH, UK

[g]Materials and Engineering Research Institute, Sheffield Hallam University, Sheffield, S1 1WB, UK

[h]College of Physics and Materials Science, Tianjin Normal University, Tianjin 300387, China

[i]School of Materials Science and Engineering, Beijing Institute of Technology, Beijing 100081, China.

*Corresponding authors. E-mail addresses:

wangdawei102@gmail.com, buaasyliu@gmail.com, i.m.reaney@sheffield.ac.uk

[#]Author contributions:

H. Ji, D. Wang, W. Bao, Z. Lu, and G. Wang contributed equally to this work.

## Abstract

Dense pseudocubic $0.62Na_{0.5}Bi_{0.5}TiO_3$-$0.3Sr_{0.7}Bi_{0.2}TiO_3$-$0.08BiMg_{2/3}Nb_{1/3}O_3$ (NBT-SBT-0.08BMN) ceramics with excellent recoverable energy density, $W_{rec}$ = 7.5 J/cm$^3$, and conversion efficiency, $\eta$ = 92%, were synthesized. Large electric breakdown strength was facilitated by electrical homogeneity, high resistivity and large activation energy (1.86 eV). Transmission electron microscopy identified the presence of polar nano-regions (PNRs) in a matrix of short coherence in-phase and antiphase octahedral tilting. Combining polar and tilt order restricted the crystal classes of PNRs to tetragonal, orthorhombic and monoclinic. Using these symmetries, the enhancement of polarization was explained using Landau-Devonshire phenomenology and percolation theory. Octahedral tilting and introduction of larger B-site ions ($Mg^{2+}$, $Nb^{5+}$) inhibited long range polar coupling, minimizing strain and maximizing $\eta$. $W_{rec}$ was further improved to 18 J/cm$^3$ (>1000 kV/cm) in multilayers whose properties were stable from 0.01–100 Hz, from 20 °C–160 °C and up to $10^6$ cycles, attractive for pulsed power applications and power electronics.



## Keywords

$Na_{0.5}Bi_{0.5}TiO_3$, capacitors, relaxors, polar nanoregions, octahedral tilting

## 1. Introduction

Consumer electronics and electrification of transportation are the main drivers for energy storage and conversion technologies such as batteries, electrochemical supercapacitors, thermoelectric devices.1-5 Beside Li-ion, Na-ion and other battery types have received attention because of the comparative scarcity of Li containing ores.6,7 Wider applications have also been reviewed by Cao et al,8-10 who have proposed several novel devices for electromagnetic energy wireless power transfer and thermoelectric energy conversion.

For direct energy storage, conventional polymer film dielectric capacitors possess inherently high power density (> 1kW/kg) along with short charge/discharge times (< 0.1 second) and are employed in pulsed power systems including motor vehicles, X-ray units, high-powered accelerators, grid-connected photovoltaics, wind turbine generators, electrochemical guns and radars.4,11-16 In contrast, multilayer ceramic capacitors (MLCCs) are mainly utilised as filters and de-couplers in consumer electronics with pulsed power applications limited by their low recoverable energy density ($W_{rec}$) and conversion efficiency ($\eta$), with respect to polymer film capacitors. Polymer film capacitors typically achieve high $W_{rec}$ due to their large electrical breakdown strength ($E_{BDS}$) but suffer from thermal and mechanical instability in comparison with MLCCs.14 Therefore, there is an urgent need to develop higher $W_{rec}$ and $\eta$ MLCCs for pulsed power applications since they have the potential to operate at high temperatures (>100 °C). Perhaps more crucially, near-engine, power electronics also require higher voltage (>300 kV/cm) and temperature (>200 °C) capacitors, the latter only realistically achievable using ceramics.4,11-16

For a dielectric, the total energy density ($W_{total}$), $W_{rec}$ and $\eta$ are given by Equations 1-3:4,11-16

$$W_{total} = \int_0^{P_{max}} E dP \quad (1)$$

$$W_{rec} = \int_{P_r}^{P_{max}} E dP \quad (2)$$

$$\eta = \frac{W_{rec}}{W_{total}} \times 100\% \quad (3)$$

where $E$, $P_{max}$ and $P_r$ are the applied electric field, maximum and remnant polarization, respectively. The equations illustrate that $W_{rec}$ and $\eta$ are optimized by both large $P_{max}$ - $P_r$ ($\Delta P$) and $E$ (electric breakdown strength, $E_{BDS}$). Current research focuses on lead-free ceramics due to concerns over PbO toxicity17,18 with anti-ferroelectrics (AFEs) and relaxor-ferroelectrics (RFEs) offering great potential as high energy density capacitors due to their large $\Delta P$.19-45 For lead-free AFEs, efforts have focused on delaying the onset of AFE-FE switching as a function of $E$ using various dopants.43 Yan et al. reported that $0.99AgNbO_3$-$0.01Bi(Zn_{2/3}Nb_{1/3})O_3$ exhibited a high $\Delta P$ of 46.8 μC/cm$^2$, resulting a large $W_{rec}$ of 4.6 J/cm$^3$ but a low $\eta$ of 57.5% under 220 kV/cm.20 Large $W_{rec}$ of 4.2 J/cm$^3$ was reported for $AgNb_{0.85}Ta_{0.15}O_3$ at 233 kV/cm also with a low $\eta$ of 69 %.21 Despite the high values of $W_{rec}$ in $AgNbO_3$-based AFEs, lower values of $\eta$ are likely due to their polarization hysteresis.20,21

For RFEs, emphasis has been placed on compositions with ultra-slim $P$-$E$ loop which do not saturate under increasing $E$. Controlled electrical homogeneity and reduced conductivity is effective in enhancing $W_{rec}$ (8.2 J/cm$^3$) in $BiFeO_3$-based RFEs 25,44,45 and high $W_{rec}$ (4.55 J/cm$^3$) and $\eta$ (90%) are also achieved for relaxor $BaTiO_3$-$0.06Bi_{2/3}(Mg_{1/3}Nb_{2/3})O_3$ ceramics.42 For $Na_{0.5}Bi_{0.5}TiO_3$ (NBT)-based compositions, high $W_{rec}$ (4.06 J/cm$^3$) and $\eta$ (87.3%) are reported for $0.65(0.84Na_{0.5}Bi_{0.5}TiO_3$-$0.16K_{0.5}Bi_{0.5}TiO_3)$-$0.35Sr_{0.7}Bi_{0.2}TiO_3$ at 350 kV/cm22 with similar results recorded by other researchers.35-41,46,47 Notably, Li et al. reported that $Na_{0.5}Bi_{0.5}TiO_3$-$Sr_{0.7}Bi_{0.2}TiO_3$ (NBT-SBT) MLCCs exhibited a then record-high $W_{rec}$ of 9.5 J/cm$^3$ with $\eta$ = 92% at 720 kV/cm.38 However, the accompanying high electrostrain in NBT-based ceramics leads to poor fatigue behavior48,49 and $E_{BDS}$ (~200 kV/cm and ~720 kV/cm for ceramics and MLCCs, respectively) still requires further enhancement to maximize $W_{rec}$.38 Therefore, we report on the design strategy and optimization of ceramic compositions for the fabrication of ultrahigh energy storage density MLCCs, accompanied by an assessment of their fatigue behavior and temperature/frequency stability.

## 2. Results and discussion

### 2.1 Crystal chemistry of an ideal high energy density relaxor ferroelectric

The key to designing an ideal RFE composition for enhanced energy density is to choose a highly polar base material (e.g. NBT or $BiFeO_3$) followed by the formation of solid solutions, in which FE long-range order is disrupted (RFE state) whilst enhancing average ionic polarizability per unit cell. In this manner, an ultra slim RFE *P-E* loop may be obtained, whose $P_{max}$ increases with increasing *E* without fully saturating, Fig. 1(a). Compositions therefore, have the potential for a large $W_{rec}$ and $\eta$, provided $E_{BDS}$ is high and there is no transition to a field induced FE state. Based on these arguments, we propose that the solid solution, (0.7-*x*)NBT-0.3SBT-*x*$BiMg_{2/3}Nb_{1/3}O_3$ (NBT-SBT-*x*BMN) is ideal for optimizing $W_{rec}$.

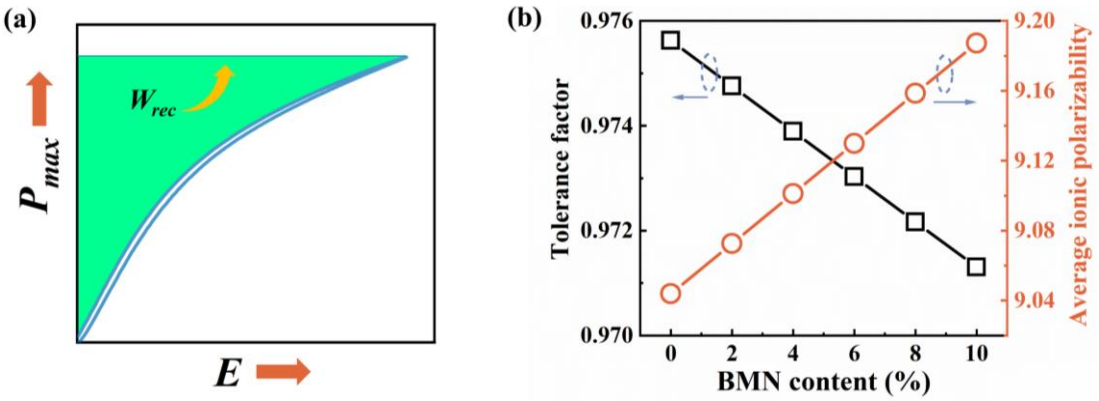


**Fig. 1.** (a) Schematic of an ideal unipolar *P-E* loop for enhancing $W_{rec}$ in RFE compositions;50 (b) tolerance factor and average ionic polarizability per unit cell of NBT-SBT-*x*BMN as a function of BMN concentration.

NBT-SBT was first studied by the authors of Li et al.38 but here we adapt compositions through a tailored dopant strategy (*x*BMN) based on our crystal chemical design principles to significantly enhance $W_{rec}$. Fig. 1(b) shows a plot of average ionic polarizability per unit cell ($\alpha$, Eq. 4)51 and perovskite tolerance factor (*t*, Eq. 5) as a function of *x* with Table S1 (ESI) giving numerical values. $\alpha$ increases whilst *t* decreases as a function of *x*.

$$\alpha(A_xB_yC_z) = x\alpha_A + y\alpha_B + z\alpha_C \quad (4)$$

where $\alpha_A$, $\alpha_B$ and $\alpha_C$ are the $\alpha$ of A, B and C ions and

$$t = \frac{R_A+R_O}{\sqrt{2}(R_B+R_O)} \quad (5)$$

where $R_A$, $R_B$ and $R_O$ are the average ionic radii of the A, B and O ions.52

NBT has intrinsic displacive competition on the A-site between Na and Bi (Fig. 1b)53 and long-range polar coupling is disrupted by forming a solid solution with SBT (Fig. 1a).38 Alloying with BMN is designed to further disrupt polar order whilst simultaneously increasing the average A-site, without sacrificing B-site, polarizability since Ti/Nb ions remain present in 95% of the O-octahedra. There is also a concomitant but small decrease in $t$ as a function of $x$ which represents an increase in the driving force for local distortions of the O sublattice through octahedral tilting.54 Hence, we can state that whilst the correlation length for polar order decreases, the driving force for octahedral tilting ($t$ decreases) and potential for off-centering of cations ($\alpha$ increases) in their respective co-ordinations increases. The combination of increased potential for off-centering through increased $\alpha$ and the further disruption in long range polar order as $x$ increases are ideal for developing RFE compositions with ultra-slim $P$-$E$ loops with enhanced $W_{rec}$ and $\eta$, Fig. 1(a). The role of octahedral tilting in defining the local symmetry of the RFE state and in suppressing the field induced transition to an FE state, reported by the authors of Li et al.38, are discussed in section 2.3 and 2.5, respectively.

### 2.2 Electrical and energy storage properties of NBT-SBT-BMN bulk ceramics

The $Z'$-$Z''$ plots for all samples at 660 °C are shown in Fig. 2(a), where $Z'$ and $Z''$ is the real and imaginary part of impedance ($Z^*$), respectively. A single arc is observed in the measured frequency range for all compositions. As BMN concentration increases, the value of the lower intercept of the arcs (i.e. total resistivity) gradually increases up to $x$ = 0.08 but decreases for $x$ = 0.1, as the solubility limit is reached (Fig. S1, ESI). Only a single peak is observed in the corresponding Z″ and M″ spectroscopic plot for $x$ = 0.08, Fig. 2(b), with further compositions

exhibiting the same behavior and presented in Fig. S2 (ESI). The data may be interpreted on an equivalent circuit with a parallel resistance-capacitance (*RC*) element, attributed to a single bulk component with $C \sim 4.87\times10^{-11}$ F/cm and resistivity of 0.25 MΩ·cm. The overlapping of the single peak in *Z″* and *M″* spectra unambiguously indicates electrical homogeneity for all compositions, which is beneficial for $E_{BDS}$.[25,45] The Arrhenius plots of total electrical conductivity ($\sigma$) for NBT-SBT-*x*BMN ceramics are displayed in Fig. 2(c), where an activation energy ($E_a$) of ~1.86 eV is obtained for all compositions. $\sigma$ decreases with increasing BMN concentration, consistent with *Z** results.

The unipolar *P-E* loops for NBT-SBT-*x*BMN ceramics at the maximum applied electric field ($E_{max}$) are shown in Fig. 2(d). The energy storage properties, $W_{rec}$ and $\eta$, for NBT-SBT-*x*BMN ceramics under $E_{max}$ are plotted in Fig. 2(e). Both $W_{rec}$ and $\eta$ are significantly enhanced with an increase in BMN concentration, with a maximum $W_{rec}$ of ~7.5 J/cm$^3$ achieved at $x$ = 0.08 with

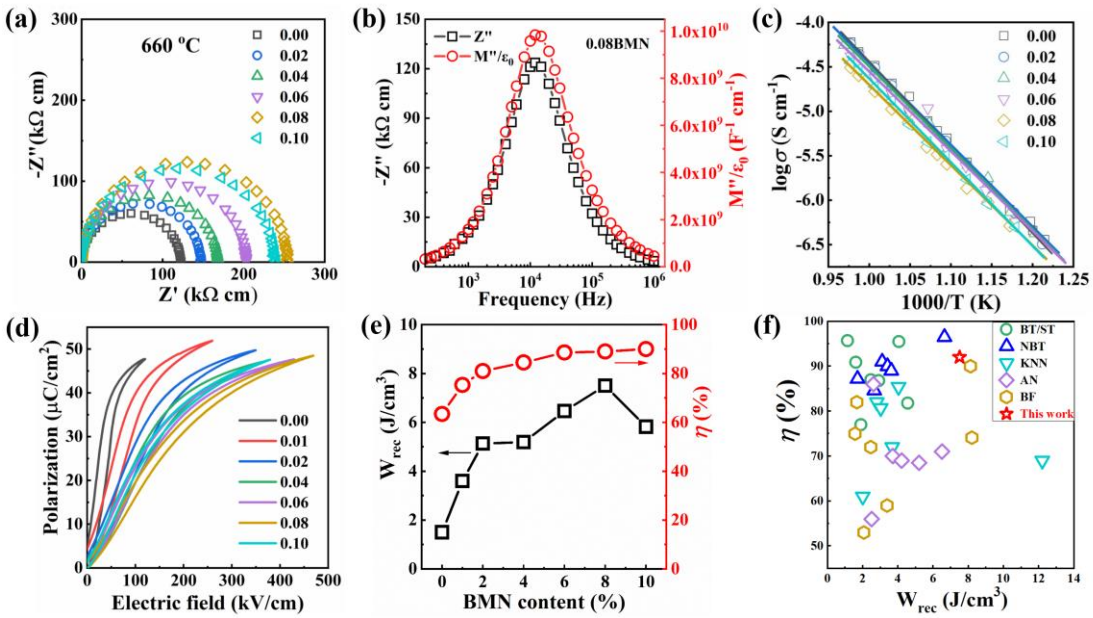


**Fig. 2.** (a) Complex AC impedance for NBT-SBT-*x*BMN at 660 °C; (b) combined *Z''* and *M''* spectroscopic plots for NBT-SBT-0.08BMN; (c) Arrhenius plots of total electrical conductivity for NBT-SBT-*x*BMN; (d) *P-E* loops at the maximum electric field, and (e) energy storage properties ($W_{rec}$ and $\eta$) for NBT-SBT-xBMN; (f) $\eta$ *vs.* $W_{rec}$ among the recently reported lead-free bulk ceramics.

$\eta$ = 92% at 470 kV/cm. Along with the large $E_{max}$, resulting from improved resistivity and electrical homogeneity (Fig. 2a-c), a large $\Delta P$ (~46 μC/cm$^2$, large $P_{max}$~48 μC/cm$^2$ and small $P_r$ ~1.5 μC/cm$^2$, Fig. S3, ESI) also contribute to the $W_{rec}$ and $\eta$, effectively describing an ideal ultra-slim *P-E* loops (Fig. 2d) which does not saturate as field increases. Comparisons of $W_{rec}$ and $\eta$ with recently reported lead-free bulk ceramics, are plotted in Fig. 2(f).[19-41,43,45,55-57] NBT-SBT-0.08BMN ceramics show the highest $W_{rec}$ of 7.5 J/cm$^3$ among all lead-free bulk ceramics together with one of the highest values of $\eta$ ~ 92%, indicating enormous potential for pulsed power and high field capacitor applications.

### 2.3. Phase and local structure of NBT-SBT-BMN bulk ceramics

Fig. S1 (ESI) shows the XRD patterns of NBT-SBT-*x*BMN ceramics (*x*=0~0.1) from 20° ~ 70° 2$\theta$, which exhibit peaks attributed to a single pseudocubic perovskite phase for $x < 0.1$, above which a secondary $Bi_2Ti_2O_7$ phase (JCPDS 32-0118) is detected. SEM images of NBT-SBT-*x*BMN ceramics are displayed in Fig. S4 (ESI), which show a dense microstructure and an average grain size of ~3 μm for all studied compositions. Raman spectra reveal an increase in the width of the characteristic modes (Fig. S5, ESI) which, in addition to broadening of permittivity ($\varepsilon_r$) maxima as a function of temperature (Fig. S6-S7, ESI), indicate that the correlation length of polar order decreases as BMN concentration increases.

Fig. 3 shows *in-situ* dark-field, two-beam superlattice TEM images obtained as a function of temperature using a ½{*hk0*} in-phase tilt reflection and the accompanying [001] selected area electron diffraction patterns for $x$ = 0.08 recorded at room temperature (RT), 100 °C and 250 °C. No FE macrodomains were observed, consistent with XRD spectra (Fig. S1, ESI), Raman data (Fig. S5, ESI) and $\varepsilon_r$ *vs*. temperature plots (Fig. S7, ESI). The $[001]_p$ ($p$ = pseudocubic) electron diffraction patterns exhibit ½{*hk0*} superstructure reflections with evidence of systematic absences (weak or absent reflections) for $h = k$, consistent with an axial glide and characteristic of in-phase tilting. Fig. S8 (ESI) is a <110> zone axis diffraction patterns which reveals ½{*hkl*}

superstructure reflections, arising from antiphase tilting, but the absence of ½{*hk0*}. For <110> zone axes, although reflections of the general type ½{*hk0*} reflections are permitted, the Weiss Zone Law dictates an extra condition such that $h = k$. For in-phase tilt reflections, $h \neq k$ and are therefore, forbidden in the <110>.

For perovskites with $t < 0.98$, (NBT-SBT-0.08BMNN, $t = 0.9722$, Table S1, ESI) combinations of in-phase and antiphase rotations are predicted based on geometric arguments by Glazer,38 and Reaney et al.54,58 The most likely explanation therefore, for the presence of ½{*hk0*} $h \neq k$ and ½{*hkl*} superstructure reflections in electron diffraction patterns is the coexistence of in-phase and antiphase tilting. Mixed tilt systems which combine in-phase and antiphase rotations are $a^+b^+c^-$, $a^+a^+c^-$, $a^+b^+b^-$, $a^+a^+a^-$, $a^+b^-c^-$, $a^+a^-c^-$, $a^+b^-b^-$, $a^+a^-a^-$, $a^0b^-b^+$ and $a^0b^-c^+$.54,58,59 Stokes et al.59 utilized group theory to combine polar displacements with mixed tilting and established 11 possible space groups, *Ama2*, *Amm2*, $Cmc2_1$, *Cc*, $P4_2mc$, *Aba2*, $Pna2_1$, $Pmc2_1$, $Pmn2_1$, *Pc*, $P2_1$ and *Pm* which therefore, describe the possible local polar structure in NBT-SBT-0.08BMN, all of which are either tetragonal (*T*), monoclinic (*M*) or orthorhombic (*O*).

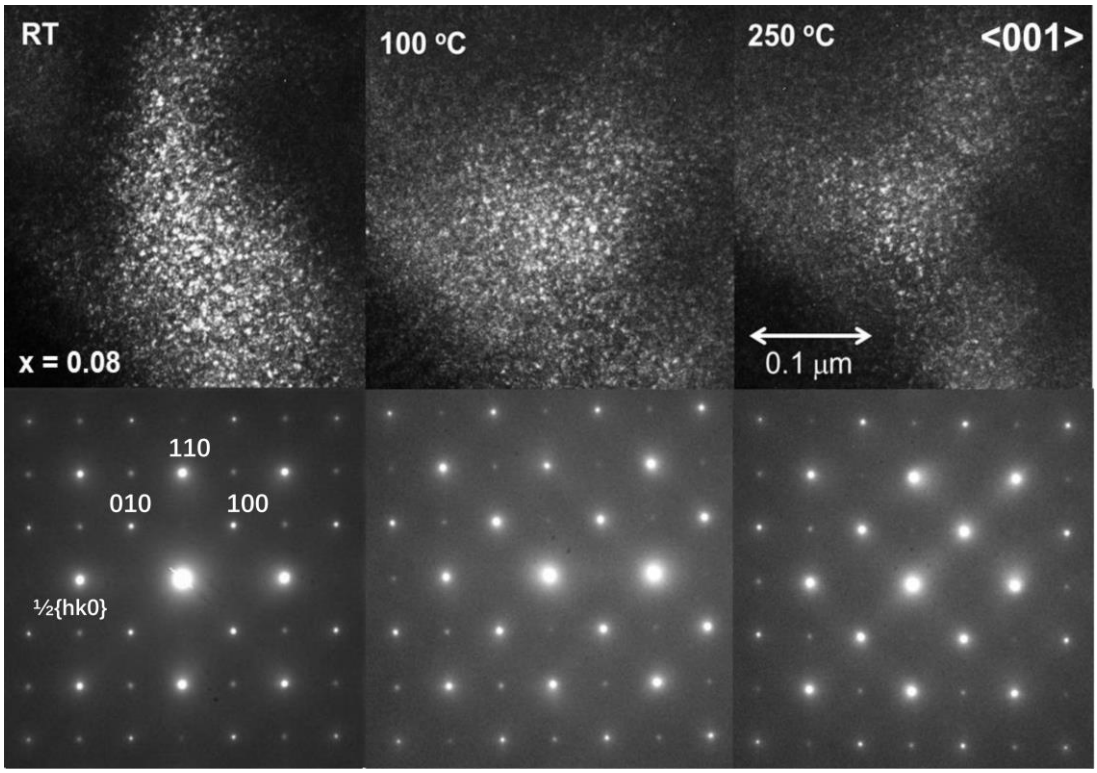

**Fig. 3.** *In-situ* dark-field, two-beam superlattice TEM images obtained using a ½{*hk0*} in-phase tilt reflection and the accompanying [001] selected area electron diffraction patterns for $x$ = 0.08 recorded at room temperature (RT), 100 °C and 250 °C.

### 2.4. Landau-Devonshire (LD) phenomenology and percolation theory

The local structure determined by TEM and electron diffraction suggests that the PNRs in $x$ = 0.08 are either *M*, *O* or *T*. However, domain boundaries constitute a large volume fraction of the matrix and act as minima for the magnitude of polarization and amplitude of tilt, thereby approximating to a cubic (*C*) state. LD phenomenology theory therefore, employs a multiphase coexistence model where *M*, *T* and *O* PNRs are embedded in a *C* (domain boundary) matrix, schematically displayed in Fig. 4(a). The three-dimensional (3D) Landau free-energy $F(\vec{P})$ schematic picture of polarization rotation in NBT-based RFEs are given in Fig. 4(e). We propose *M* state acts as an intermediate phase/structural bridge between *T* and *O* phase, which allows the polarization vector to rotate within the (010) plane. The $F(\vec{P})$ of rhombohedral (*R*) phase is much higher than that of *T*, *M* and *O*, which indicates that *T*, *M* and *O* PNRs are more likely. Also, only a small energy barrier of polarization rotation between the *T*, *M* and *O* states is observed, leading to easy polarization rotation along <100> *T* and <110> *O* directions under weak stimuli. The Landau $F(\vec{P})$ curve of polarization extension for *T*, *M* and *O* polarization directions are plotted in Fig. 4(f), where a small energy barrier for the polarization extension is observed between the paraelectric (*C*) and ferroelectric (*T*, *M* or O) phases. When a *E* is applied, the $F(\vec{P})$ is lowered as shown in Fig. 4(f), indicating a high response by polarization extension.

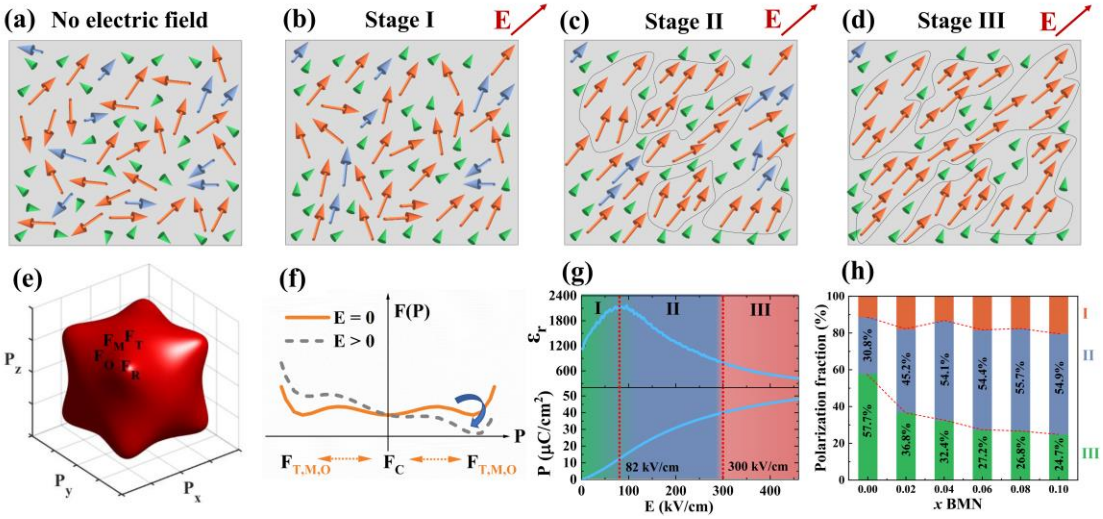


**Fig. 4.** Schematic of PNRs in the cubic matrix for NBT-SBT-BMN RFEs: (a) original stage without *E*, (b) Stage I: polarization rotation and extension with a small *E*, (c) Stage II: PNR percolation with a medium *E*, (d) Stage III: polarization enhancement with a large *E*; (e) 3D Landau free-energy profile of polarization rotation with different polarization directions; (f) 2D Landau free-energy curve of polarization extension without and with *E*; (g) three stages in the $\varepsilon_r$/*P*-*E* loops of NBT-SBT-0.08BMN; (h) polarization fraction of each stage for studied NBT-SBT-*x*BMN.

According to the field-induced micro-macro domain transition (MMDT) model,60 the small energy barrier of polarization rotation and extension in NBT-SBT-0.08BMN leads to easy re-orientation and re-arrangement of PNRs along or close to the direction of *E* (named Stage I: polarization rotation and extension, Fig. 4b), which results in a rapid increase of both polarization and $\varepsilon_r$ under a small *E*, as shown in Fig. 4(g). As *E* increases, some PNRs merge to form larger clusters with dipoles lying approximately along the direction of *E* enhancing polarization and reducing $\varepsilon_r$ (Stage II: PNR percolation),61 Fig. 4(c) and (g). Finally, polarization continues to increase with *E*, resulting in an increase in the dipolar intensity (Stage III), Fig. 4(d) and (g). The nonlinear curve of polarization as a function of *E* (Fig. 4g and Fig. S9, ESI) is attributed to the different underlying mechanisms of each stage.61 However, the dominant contribution to polarization gradually changes from Stage I (polarization rotation and extension) for NBT-SBT (~30 of total 52 μC/cm$^2$, 57.7%) to Stage II (PNR percolation, ~27 of

total 48 μC/cm$^2$, 55.7%) as BMN concentration increases, Fig. 4(h) and Fig. S9 (ESI).

### 2.5. Ultrahigh energy storage properties in NBT-SBT-BMN MLCCs

Single-layer MLCCs were fabricated from NBT-SBT-0.08BMN to decrease the dielectric layer thickness and thereby improve $E_{BDS}$.[24-27] Secondary and back scattered electron (SEM/BSE) images, elemental energy dispersive X-ray (EDX) mapping/line of a cross-section of the MLCCs are given in Fig. 5(a) and Fig. S10 (ESI). The thickness of dielectric layer and Pt inner electrode is ~7 μm and ~3.5 μm, respectively. No delamination, wrapping or mechanical defects are observed. Fig. 5(b) and (c) are bright field and filtered high resolution TEM images, respectively obtained from the interface between an NBT-SBT-0.08BMN ceramic and Pt electrode which indicate the presence of a Bi deficient intermediate layer. A bright field scanning-TEM (STEM) image and corresponding EDX maps are shown in Fig. S11 (ESI), which further indicates limited inter-reaction through the formation of a Bi-deficient between NBT-SBT-0.08BMN ceramic and Pt electrode.

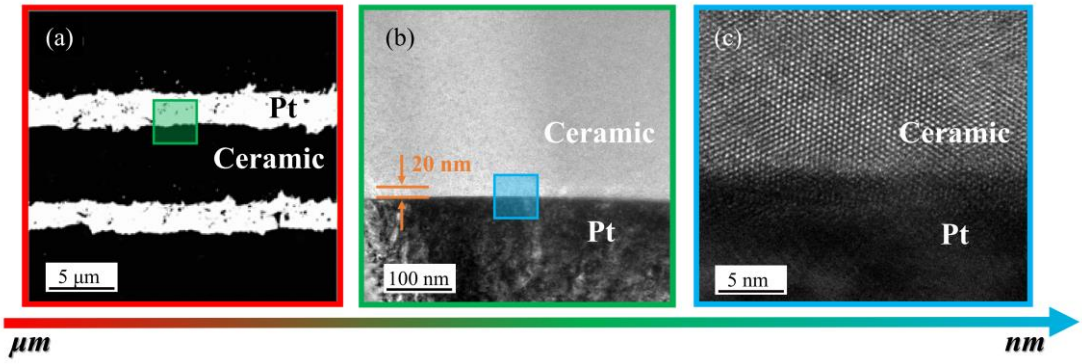


**Fig. 5.** (a) Cross-sectional BSE image; (b) TEM micrograph obtained from an interface between an NBT-SBT-0.08BMN grain and a Pt grain (electrode); (c) HRTEM image (filtered) obtained from the interface at a higher magnification.

The unipolar *P-E* loops of NBT-SBT-0.08BMN MLCCs as a function of *E*, temperature, frequency and cycling are shown in Fig. S12 (ESI), respectively. The corresponding energy storage performance is calculated and plotted in Fig. 6(a-d). $E_{max}$ increases to 1013 kV/cm compared with 470 kV/cm for bulk samples, due to the reduction of dielectric layer thickness

(~7 μm).24-27 At $E_{max}$ (1013 kV/cm), $P_{max}$ = 53.8 μC/cm$^2$ with $P_r$ only 1.1μC/cm$^2$ yielding ultrahigh $W_{rec}$ (18 J/cm$^3$) and $\eta$ (93%), Fig. 6(a). The MLCCs exhibit excellent temperature stability ($W_{rec}$ varies < 15% from 20 °C to 160 °C), frequency stability ($W_{rec}$ varies <10%, 0.01 Hz-100 Hz) and fatigue resistance (< 3% over for $10^6$ cycles), Fig. 6(b-d), attractive for practical applications. The excellent fatigue resistance is attributed to low hysteresis and electrostrain due to the absence of an electric-field induced phase transition in undoped NBT-SBT with respect to BMN-doped compositions (Fig. 7 and Fig. S13, ESI), which decreases cracking and thermal breakdown during cycling.

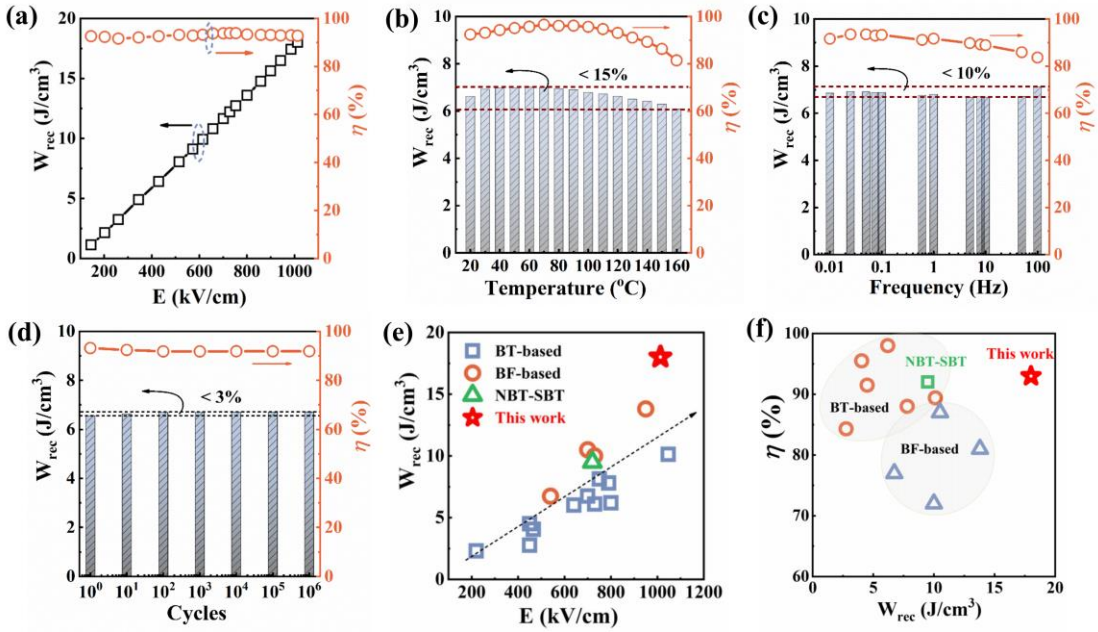


**Fig. 6**. Energy storage properties for NBT-SBT-0.08BMN MLCCs with the increase of (a) electric field, (b) temperature, (c) frequency and (d) cycle number; (e) comparison of $W_{rec}$ as a function of $E_{max}$, and (f) comparison of $W_{rec}$ and $\eta$ among recently reported lead-free MLCCs.

Zhang and co-workers 62 utilized $SrTiO_3$ seeds to orient grains in the fabrication of multilayers of NBT-SBT and achieved an enhancement of $W_{rec}$ to ~21 J/cm$^3$ but with a relatively lower $\eta$ (~80%) (here we report $\eta$ = 93%). However, electrostrain due to the field-induced transition was >0.15% and the impracticality of producing oriented multilayers in mass production severely reduces the impact of this research.62 The lower electrostrain in BMN-doped in comparison with undoped compositions (Fig. 7 and Fig. S13, ESI) relates to the absence of a

field induced transition to a long range ordered FE state. The suppression of a field induced FE state is attributed to a decrease in polar coupling through the incorporation of larger Mg and Nb in comparison with Ti ions on the B-site. This increases the energy barrier to long range coalescence of PNRs under *E*. The presence of short range ordered tilted regions is also considered to increase the energy barrier for coalescence of PNRs since the local polarization vectors are coupled to distortions of the octahedral sub-lattice which are known to increase the energy for domain wall motion by suppressing polarization rotation in piezoelectric ceramics.[63] In summary therefore, we propose that NBT-SBT-0.08BMN MLCCs which exhibit $W_{rec}$ (~18 J/cm$^3$) together with $\eta$ (93%) represent a step change in high energy density capacitors as summarized in our comparison of polycrystalline (non-oriented) systems in Fig. 6(e,f).[24-28,38,64-68]

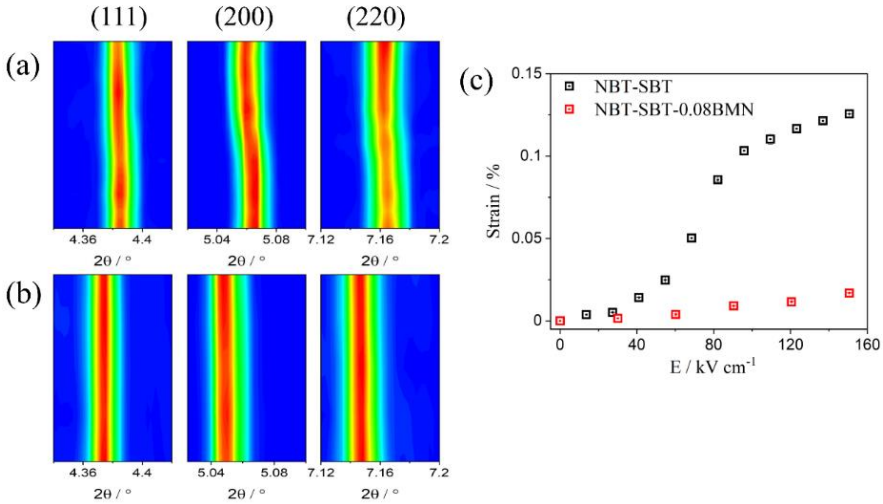


**Fig. 7.** Changes of synchrotron XRD representative peaks for (a) NBT-SBT and (b) NBT-SBT-0.08BMN at Ψ=0° (along with electric field direction) under application of electric field up to 150 kV cm$^{-1}$. (c) calculated strain from the synchrotron XRD.

## 3. Conclusions

NBT-SBT-*x*BMN ($0 \leq x \leq 0.1$) ternary lead-free ceramics were fabricated by conventional solid-state reaction technique. For $x < 0.1$, a single pseudocubic perovskite phase was observed for which resistivity gradually increased with BMN concentration. Samples were also electrically homogeneous with high activation energy for conductivity, leading to enhancement of $E_{BDS}$ and

$W_{rec}$ = 7.5 J/cm$^3$ and $\eta$ = 92% for $x$ = 0.08 at 470 kV/cm. TEM, XRD, $\varepsilon_r$ *vs.* temperature and Raman spectroscopy indicated that the correlation length of polar order decreased with increasing BMN concentration. This was accompanied by a decrease in $t$ but an increase in $\alpha$, leading to the formation of PNRs within a matrix of short coherence in-phase and antiphase tilting. The short-range tilt order in combination with the inclusion of larger B-site ions was considered to inhibit the formation of a long-range FE phase under $E$, resulting in minimal strain and an ultra-slim $P$-$E$ which optimizes $\eta$ and $P_{max}$. Optimization of polarization was explained using Landau-Devonshire phenomenology and percolation theory based on a $C$ matrix containing $O$, $T$ and $M$ phases, predicted to be present by combining local polar order with mixed in-phase/antiphase tilting. A further increase in $W_{rec}$ to 18 J/cm$^3$ was achieved in MLCCs due to a reduction of dielectric layer thickness which increased $E_{BDS}$. The MLCCs also displayed excellent frequency stability (0.01–100 Hz), temperature stability (20–160 °C) and fatigue endurance (>10$^6$ cycles), demonstrating that BNT-BST-0.08BMN has exceptional potential for pulsed power and high voltage capacitor applications.

**Acknowledgements**

This work was supported by the EPSRC (EP/L017563/1 and EP/N010493/1), Henry Royce Institute for Advanced Materials, funded through EPSRC (EP/R00661X/1, EP/S019367/1, EP/P02470X/1 and EP/P025285/1) and National Natural Science Foundation of China (61601359). We thank Dr. Zhongming Fan from Materials Research Institute of The Pennsylvania State University to discuss the percolation theory.

**Conflicts of interest**

The authors declare no competing interest.

**Data and materials availability**

The data that support the findings are available from the corresponding authors upon request.

## References


1. Zhang, X., *et al.*, *Energy Environmental Science* (2019) **12** (6), 1918
2. Yu, Z., *et al.*, *Advanced Functional Materials* (2019) **29** (1), 1806799
3. Wang, S., *et al.*, *Advanced Energy Materials* (2016) **6** (13), 1600137
4. Palneedi, H., *et al.*, *Advanced Functional Materials* (2018) **28** (42), 1803665
5. Lin, Y., *et al.*, *Journal of Materials Chemistry A* (2020) **8** (44), 23427
6. Chen, L. L., *et al.*, *Adv Mater* (2020) **32** (42), e2001212
7. Zhang, X., *et al.*, *Energy & Environmental Science* (2019) **12** (6), 1918
8. Cao, M., *et al.*, *Small* (2018), e1800987
9. Cao, M. S., *et al.*, *Advanced Functional Materials* (2019) **29** (25)
10. Shu, J. C., *et al.*, *Advanced Functional Materials* (2020) **30** (10)
11. Han, F., *et al.*, *Science Advances* (2015) **1** (9), e1500605
12. Yao, Z., *et al.*, *Advanced Materials* (2017) **29** (20), 1601727
13. Thakur, V. K., and Gupta, R. K., *Chemical Reviews* (2016) **116** (7), 4260
14. Li, Q., *et al.*, *Annual Review of Materials Research* (2018) **48**, 219
15. Yang, L., *et al.*, *Progress in Materials Science* (2019) **102**, 72
16. Sun, Z., *et al.*, *Advanced Electronic Materials* (2020) **6** (1), 1900698
17. Ibn-Mohammed, T., *et al.*, *Energy Environmental Science* (2016) **9** (11), 3495
18. Wang, D., *et al.*, *Journal of Advanced Dielectrics* (2018) **8**, 1830004
19. Liu, G., *et al.*, *Ceramics International* (2019) **45** (15), 19189
20. Yan, Z., *et al.*, *Journal of Materials Chemistry A* (2019) **7** (17), 10702
21. Zhao, L., *et al.*, *Advanced Materials* (2017) **29** (31), 1701824
22. Hu, D., *et al.*, *Journal of Materials Chemistry C* (2020) **8**, 591
23. Wang, D., *et al.*, *ACS Applied Energy Materials* (2018) **1** (8), 4403
24. Wang, D., *et al.*, *Journal of Materials Chemistry A* (2018) **6** (9), 4133
25. Wang, G., *et al.*, *Energy Environmental Science* (2019) **12** (2), 582
26. Wang, G., *et al.*, *Journal of Materials Chemistry A* (2020) **8**, 11414
27. Wang, G., *et al.*, *Journal of the European Ceramic Society* (2020) **40** (4), 1779
28. Li, W.-B., *et al.*, *ACS Applied Energy Materials* (2019) **2** (8), 5499
29. Liu, G., *et al.*, *Chemical Engineering Journal* (2020) **398**, 125625
30. Zhang, L., *et al.*, *Journal of the European Ceramic Society* (2019) **39** (10), 3057
31. Li, W.-B., *et al.*, *Journal of Materials Chemistry A* (2017) **5** (37), 19607
32. Zhang, L., *et al.*, *Journal of the European Ceramic Society* (2020) **40** (8), 3343
33. Yuan, Q., *et al.*, *Nano Energy* (2018) **52**, 203
34. Huang, Y. H., *et al.*, *Journal of Materials Chemistry A* (2018) **6** (10), 4477
35. Pan, Z., *et al.*, *Journal of Materials Chemistry C* (2019) **7** (14), 4072
36. Yang, L., *et al.*, *Journal of Materials Chemistry A* (2019) **7** (14), 8573
37. Wu, J., *et al.*, *Nano Energy* (2018) **50**, 723
38. Li, J., *et al.*, *Advanced Materials* (2018) **30** (32), 1802155
39. Qi, H., and Zuo, R., *Journal of Materials Chemistry A* (2019) **7** (8), 3971
40. Wu, Y., *et al.*, *Journal of Materials Chemistry C* (2019) **7** (21), 6222
41. Qiao, X., *et al.*, *Journal of Materials Chemistry C* (2019) **7** (34), 10514

42. Yang, H.-J., *et al.*, *ACS Applied Materials Interfaces* (2020) **12**, 43942
43. Lu, Z., *et al.*, *Nano Energy* (2021) **79**, 105423
44. Wang, G., *et al.*, *Journal of Materials Chemistry A* (2020) **8** (22), 11414
45. Lu, Z., *et al.*, *Energy Environmental Science* (2020) **13**, 2938
46. Li, D., *et al.*, *Chemical Engineering Journal* (2020) **392**, 123729
47. Yan, F., *et al.*, *Energy Storage Materials* (2020) **30**, 392
48. Zhang, S. T., *et al.*, *Advanced Materials* (2009) **21** (46), 4716
49. Jo, W., *et al.*, *Journal of Electroceramics* (2012) **29** (1), 71
50. Zhou, M., *et al.*, *Journal of Materials Chemistry A* (2018) **6** (37), 17896
51. Shannon, R. D., *Journal of Applied Physics* (1993) **73** (1), 348
52. Shannon, R. D., *Acta Crystallographica Section A* (1976) **32** (5), 751
53. Levin, I., and Reaney, I. M., *Advanced Functional Materials* (2012) **22** (16), 3445
54. Reaney, I. M., *et al.*, *Japanese Journal of Applied Physics* (1994) **33** (7R), 3984
55. Qi, H., *et al.*, *Advanced Energy Materials* (2020) **10** (6), 1903338
56. Qi, H., *et al.*, *Advanced Functional Materials* (2019) **29** (35), 1903877
57. Yan, F., *et al.*, *Nano Energy* (2020) **75**, 105012
58. Glazer, A., *Acta Crystallographica Section B* (1972) **28** (11), 3384
59. Howard, C. J., and Stokes, H. T., *Acta Crystallographica Section B* (1998) **54** (6), 782
60. Xi, Y., *et al.*, *Journal of Applied Physics* (1983) **54** (6), 3399
61. Prosandeev, S., *et al.*, *Physical Review Letters* (2013) **110** (20), 207601
62. Li, J., *et al.*, *Nature Materials* (2020)
63. Zheng, H., *et al.*, *Journal of the American Ceramic Society* (2002) **85** (9), 2337
64. Ogihara, H., *et al.*, *Journal of the American Ceramic Society* (2009) **92** (8), 1719
65. Chen, L., *et al.*, *Journal of the American Ceramic Society* (2019) **102** (7), 4178
66. Zhao, P., *et al.*, *Advanced Energy Materials* (2019) **9** (17), 1803048
67. Cai, Z., *et al.*, *Applied Physics Letters* (2019) **115** (2), 023901
68. Li, W.-B., *et al.*, *ACS Applied Energy Materials* (2018) **1** (9), 5016
69. Liu, S. Y., *et al.*, *Journal of the American Ceramic Society* (2016) **99** (10), 3336
70. Daymond, M. R., *Journal of Applied Physics* (2004) **96**, 4263

## Experimental

### Ceramic and capacitor fabrication

$(0.7\text{-}x)Na_{0.5}Bi_{0.5}TiO_3\text{-}0.3Sr_{0.7}Bi_{0.2}TiO_3\text{-}xBiMg_{2/3}Nb_{1/3}O_3$ ($x$=0, 0.02, 0.04, 0.06, 0.08, 0.1) ceramics (abbreviated as NBT-SBT-$x$BMN) were fabricated by solid state reaction. Analytical-grade oxides or carbonates, $Na_2CO_3$ (99.95%), $SrCO_3$ (99.9%), $Bi_2O_3$ (99.9%), $TiO_2$ (99.9%), MgO (99.5%) and $Nb_2O_5$ (99.5%) were dried for 12 h to remove the absorbed water, weighed according to the stoichiometric formula and ball-milled 12 h with isopropanol. After milling, the mixed chemicals were dried 12 h at 80 °C. The powders were subsequently calcined 3 h at 900 °C in alumina crucibles and re-milled 12 h. After drying, they were pressed into pellets

with 8 mm in diameter and 1 mm in thickness at 100 MPa. To compensate for evaporation of Na and Bi oxide during sintering, green pellets were embedded in precursor powders of the same composition and sintered 2 h at 1190-1200 °C. MLCCs were fabricated by tape-casting of NBT-SBT-0.08BMN, followed by screen-printing, stacking, lamination, co-sintering and termination, as reported previously.[24-27,45]

**Characterization**

Sintered samples were measured using the Archimedes method with relative densities >95% achieved for all ceramics. The average crystal structure was determined at room temperature using a Bruker D2 phaser X-ray diffractometer (XRD) with a Cu$K\alpha$ radiation ($\lambda$ = 0.15406 nm). The surface morphology and elemental distribution was examined using a FEI Inspect F50 scanning electron microscope (SEM) with a backscattered electron (BSE) detector. Ceramic specimens were ground, polished and then ion milled for transmission electron microscopy (TEM). A JEOL-2100F microscope was used for obtain high resolution images, electron diffraction patterns and energy dispersive X-ray analysis. To measure electrical properties, both sides of polished samples were coated with a gold electrode paste, then fired 2 h at 850 °C. Dielectric properties were measured from 30 to 600 °C using an Agilent 4980 LCR meter (Santa Clara, CA, USA). Polarization-Electric field (*P*-*E*), Strain-Electric field (*S*-*E*) and Current-Electric field (*I*-*E*) loops were measured using an aixACCT TF-2000 ferroelectric analyzer (Aachen, Germany). Samples for *P*-*E* loops measurement were polished to ~0.15mm thickness with electrodes deposited smaller than the specimen surface area to prevent breakdown along the vertical edge.

Variable complex impedance spectra were obtained using an Agilent 4184 A precision LCR meter (Pala-Alto, CA, USA). High-energy synchrotron XRD *in-situ* poling experiments were performed at beamline I15 Diamond light source with a photon energy of 72 keV and a wavelength of 0.1722 Å. Ceramic pellets were cut into bars with dimension of L5 × W1 × H1

mm, annealed for 4 h at 700 °C and gold sputtered on the top and bottom side to form electrodes. The X-ray beam was focused to 70 μm in diameter directly in front of the sample. The bar-shape specimens were placed in silicone oil in a custom-designed polyimide sample holder and electrically connected with a high voltage amplifier (Matsusada EC-10) during measurements. The *in-situ* XRD was performed in transmission mode and patterns were collected using a PerkinElmer XRD 1621 flat-panel detector. The lattice strain for each individual peak can be calculated based on the peak position. The electric field induced strain is estimated using the weighted-average strain of individual {*hkl*} planes, as introduced by Daymond as follows.70

$$\varepsilon = \frac{\sum_{hkl} T_{hkl} m_{hkl} \varepsilon_{hkl}}{\sum_{hkl} T_{hkl} m_{hkl}} \quad (6)$$

where $\varepsilon_{hkl}$ is the strain for the {*hkl*} orientation, $T_{hkl}$ is the texture index, and $m_{hkl}$ are multiplicities of crystal {*hkl*} planes, respectively.

**Landau-Devonshire phenomenology theory**

To explain the energy storage performance in NBT-based RFEs, Landau-Devonshire (LD) thermodynamic theory within the 6th-order terms of polarization was employed. The free energy of a ferroelectric is expressed by the polarization components ($P_x$, $P_y$, $P_z$).69

$$\begin{aligned} F(\vec{P}) &= F_0 + \alpha(P_x^2 + P_y^2 + P_z^2) + \beta_1(P_x^4 + P_y^4 + P_z^4) \\ &+ \beta_2(P_x^2P_y^2 + P_y^2P_x^2 + P_z^2P_x^2) + \gamma_1(P_x^6 + P_y^6 + P_z^6) \\ &+ \gamma_2[P_x^4(P_y^2 + P_z^2) + P_y^4(P_z^2 + P_x^2) + P_z^4(P_x^2 + P_y^2)] + \gamma_3 P_x^2P_y^2P_z^2, \end{aligned} \quad (7)$$

where parameters $\alpha$, $\beta_1$, $\beta_2$, $\gamma_1$, $\gamma_2$, and $\gamma_3$ are the coefficients of different orders of polarization $P$. $F(\vec{P})$ is the free energy at a certain temperature and composition as a function of polarization. $F_0$ is the free energy of a paraelectric phase. For our multiphase coexistence model with tetragonal (T), orthorhombic (O) and cubic (C) phases, the free energy of each phase is considered to be the same, and the first deviation of the free energy for a certain phase is zero to achieve stability. We can then thus write,

$$F(\overrightarrow{P_T}) = F(\overrightarrow{P_O}) = F(\overrightarrow{P_C}) = F_0, \quad (8)$$

and

$$\partial F(\vec{\mathrm{P}})/\partial(\vec{\mathrm{P}}) = 0 \quad (\text{at } \vec{P}=\vec{P_{\mathrm{T}}}\ ,\ \vec{P}=\vec{P_{O}}\ ) \tag{9}$$

where

$$\vec{P_{\mathrm{T}}} = P_0 * (0,0,1) \quad \text{and} \quad \vec{P_{\mathrm{O}}} = P_0 * (0, \tfrac{1}{\sqrt{2}}, \tfrac{1}{\sqrt{2}})\,.$$

based on Eqs. (5) and (6), the free energy can then be rewritten as

$$F(\vec{P}) = F_0 + \gamma_1 P_0^4 P^2 - 2\gamma_1 P_0^2 P^4 + \gamma_1 P^6 + (\gamma_3 - 6\gamma_1) P_x^2 P_y^2 P_z^2, \tag{10}$$

where $P^2 = P_x^2 + P_y^2 + P_z^2$.

Click here to access/download
**Supplementary Material**
NBT-SBT-BMN-supplementary information-2020-11-11.docx